JOURNAL OF MARINE RESEARCH

The *Journal of Marine Research,* one of the oldest journals in American marine science, published important peer-reviewed original research on a broad array of topics in physical, biological, and chemical oceanography vital to the academic oceanographic community in the long and rich tradition of the Sears Foundation for Marine Research at Yale University.

An archive of all issues from 1937 to 2021 (Volume 1–79) are available through EliScholar, a digital platform for scholarly publishing provided by Yale University Library at https://elischolar.library.yale.edu/.

Requests for permission to clear rights for use of this content should be directed to the authors, their estates, or other representatives. The *Journal of Marine Research* has no contact information beyond the affiliations listed in the published articles. We ask that you provide attribution to the *Journal of Marine Research.*

Journal of

MARINE RESEARCH

Wind-driven secondary circulation in ocean mesoscale

by Dong-Kyu Lee[1], Peter Niiler[1], Alex Warn-Varnas[2] and Steve Piacsek[3]

ABSTRACT

A two-dimensional, numerical circulation model is used to study the response of a stratified, f-plane ocean current to wind stress forcing at the surface. Nonhydrostatic, primitive equations are integrated on a 3 m vertical and 400 m horizontal grid in a periodic domain perpendicular to the ocean current. Initially, a geostrophically balanced current $[V_i(x, z)]$ with a maximum Rossby number of 0.16–0.8 is maintained against horizontal and vertical diffusion by a body force. A spatially uniform wind is applied along and across this jet. A secondary circulation is created as a result of the nonlinear interaction between the jet and wind-driven flow in the Ekman layer. We present results from seven numerical experiments.

When the wind blows in the direction of the jet (against the jet), a narrow upwelling (downwelling) area and broad downwelling (upwelling) area are formed. This secondary circulation pattern extends well below the mixed layer. When the wind blows perpendicular to the jet, the secondary circulation does not extend below the mixed layer. The fully nonlinear secondary circulation is 50% weaker than the circulation produced by the semi-linearized calculation around the basic state, V_i. Near-inertial fluctuations appear and are confined to the negative relative vorticity side of the circulation ($d\bar{V}/dx < 0$). The time-averaged vertical velocity can be as high as 1.5 m/day with a wind stress of 1 dyne/cm^2 over a jet and a maximum Rossby number of 0.16. The magnitude of the vertical circulation in this symmetric basic state is dependent on the Rossby number and the horizontal and vertical mixing coefficients.

1. Introduction

How do wind-driven motions in the mixed layer interact with pre-existing oceanic velocity structures? Experimental evidence of such interactions has been presented

---

1. Scripps Institution of Oceanography, University of California, La Jolla, California, 92093, U.S.A.
2. Saclant Research Center, AE 09613, U.S.A.
3. Naval Research Lab., Code 7322, Stennis Space Center, Mississippi, 39529, U.S.A.

by Weller (1982, 1985) and Kunze (1985). The results from their experiments, which were designed to investigate the interactions between a wind-driven inertial motion and a slowly changing velocity deformation field, show that the effective inertial frequency is modified by the low frequency deformation field and that the inertial motions are trapped in the regions that have a minimum modified inertial frequency.

Niiler (1969) suggests the simplest theoretical basis for linear interaction of a steady Ekman layer and ocean mesoscale. In his analytical solution of the linearized, wind driven flow about a barotropic ocean current with a finite Rossby number, he has shown that a uniform wind stress (τ) in the direction of a barotropic current (V_i), acting on an ocean with constant Coriolis parameter f, causes the Ekman layer transport to be perpendicular to the current and equal to $\tau/(f + V_{ix})$. Therefore, the Ekman layer divergence, or the vertical velocity beneath the Ekman layer, is equal to $-\tau \cdot V_{ixx}/(f + V_{ix})^2$. On the positive (negative) shear side of the current, the Ekman transport decreases (increases). Consequently, a strong localized upwelling regions is found in an area beneath the axis of the jet where V_{ixx} is large and negative; and, weaker downwelling areas are found on the rims of the jet.

In another study, Klein and Hua (1988) have considered an upper ocean deformation field with a small Rossby number. They have evaluated the vertical velocity beneath the Ekman layer using linear perturbation theory on a wind driven flow perturbed about a barotropic component of a quasi-geostrophic (QG) eddy field. This calculation is identical to Niiler's (1969) model if the mesoscale consists of unidirectional jets. The analytical expression for the vertical velocity is used as an additional term in the entrainment equation, and the mixed layer equations of Pollard *et al.*'s (1973) bulk model are integrated forward in time for the mixed layer depth at each grid point of the QG model. After two inertial periods, the two-dimensional field of the mixed-layer depth has a horizontal structure that is congruous with the vorticity gradient of the QG mesoscale parallel to the wind.

The results of these linear calculations led us to consider a more complete model in which we could directly compute the three-dimensional circulation. We are interested in the structure of the vertical velocity not only within the mixed layer but throughout the entire stratified, yet diffusive water column. How does the introduction of vertical advection beneath the mixed-layer change the overall circulation patterns both above and within the mixed layer? Because the Ekman layer has a large vertical shear, any introduced vertical advection can cause increased transport of momentum and diffusion between the mixed layer and the lower stratified layer. The previous calculations (Niiler, 1969; Klein and Hua, 1988) did not show such an effect.

We want to know the magnitude of the vertical velocity and the deficiencies of the linearized model of these phenomena. Only a detailed numerical computation throughout the water column can answer these questions. Our results show that in a mesoscale current, even with a small Rossby number, the vertical advection of

horizontal momentum is so large that neither quasi-linear decomposition nor adding a wind-driven Ekman layer onto the geostrophic layer is realistic.

In this paper a nonhydrostatic, primitive equation model is used to study the interaction between a wind-driven current and a pre-existing flow on the stratified, f-plane ocean. Solutions are presented with the wind direction either perpendicular or parallel to the current.

The details of the model are described in Section 2, with a simple Richardson number-dependent vertical mixing coefficient in the mixed layer and constant diffusion below the mixed layer. The results of the integration are presented in Section 3 and the discussions and summary are in Section 4 and Section 5, respectively.

2. Model

The model is a 2-½-dimensional (in x-z coordinate with y component of velocity), nonhydrostatic, primitive equation model. The model domain is 40 km wide and 300 m deep with a periodic boundary condition in the x direction, and vanishing vertical velocities at the surface and bottom. The vertical mixing is Richardson number-dependent with a maximum vertical eddy diffusivity of 200 cm²/s. The grid resolution is 400 m in the horizontal and 3 m in the vertical. The maximum initial Rossby number depends upon the speed of the initial jet and ranges from 0.16 to 0.8. Secondary circulation is driven by an applied wind stress at the surface. A description of the model with these boundary and initial conditions is presented below. The nondimensionalized momentum equations are derived in the Appendix to demonstrate the scales resolved in the model.

a. The governing equations. The basic equations of the model use the Boussinesq approximation to the equation of motion on a rotating Cartesian plane. The governing equations are:

$$\frac{\partial u}{\partial t} + u\frac{\partial u}{\partial x} + w\frac{\partial u}{\partial z} - fv = -\frac{1}{\rho_o}\frac{\partial P}{\partial x} + \frac{\partial}{\partial x}\left(\frac{1}{\rho_o}\tau_{xx}\right) + \frac{\partial}{\partial z}\left(\frac{1}{\rho_o}\tau_{xz}\right) \tag{1}$$

$$\frac{\partial v}{\partial t} + u\frac{\partial v}{\partial x} + w\frac{\partial v}{\partial z} + fu = -\frac{1}{\rho_o}\frac{\partial \hat{P}}{\partial y} + \frac{\partial}{\partial x}\left(\frac{1}{\rho_o}\tau_{yx}\right) + \frac{\partial}{\partial z}\left(\frac{1}{\rho_o}\tau_{yz}\right) + F_v \tag{2}$$

$$\frac{\partial w}{\partial t} + u\frac{\partial w}{\partial x} + w\frac{\partial w}{\partial z} + g\frac{\rho}{\rho_o} = -\frac{1}{\rho_o}\frac{\partial P}{\partial z} + \frac{\partial}{\partial x}\left(\frac{1}{\rho_o}\tau_{zx}\right) + \frac{\partial}{\partial z}\left(\frac{1}{\rho_o}\tau_{zz}\right) \tag{3}$$

$$\frac{\partial u}{\partial x} + \frac{\partial w}{\partial z} = 0 \tag{4}$$

$$\frac{\partial T}{\partial t} + u\frac{\partial T}{\partial x} + \frac{\partial T}{\partial z} = K_H\frac{\partial^2 T}{\partial x^2} + \frac{\partial}{\partial z}K_v\frac{\partial T}{\partial z} + F_\rho, \tag{5}$$

$$\rho = -\alpha g T \tag{6}$$

where, in standard notion:

(u, v, w) = the (x, y, z) components of velocity

$f = 1.0 \times 10^{-4}/\text{sec}$ = Coriolis parameter

$g = 980 \text{ cm/sec}^2$ = acceleration of gravity

$\rho_o + \rho(x, z, t)$ = total density

$T(x, z, t)$ = temperature

$\alpha = 0.2 \times 10^{-3}\,^\circ\text{C}^{-1}$ = thermal expansion coefficient

$P(x, z)$ = pressure

$\dfrac{1}{\rho_o}\dfrac{\partial \hat{P}}{\partial y}$ = uniform pressure gradient in y direction required for stable solution

and

(F_v, F_ρ) = forcing terms.

The turbulent Reynolds stresses are expressed as,

$$\frac{1}{\rho_o}\tau_{xx} = A_H\frac{\partial u}{\partial x}$$

$$\frac{1}{\rho_o}\tau_{xz} = A_V\left(\frac{\partial u}{\partial z} + \frac{\partial w}{\partial x}\right)$$

$$\frac{1}{\rho_0}\tau_{yx} = A_H\frac{\partial v}{\partial x}$$

$$\frac{1}{\rho_o}\tau_{yz} = A_V\frac{\partial v}{\partial z}$$

$$\frac{1}{\rho_o}\tau_{zz} = A_{Vo}\frac{\partial w}{\partial z}$$

where A_H and K_H are the constant horizontal turbulent viscosity and heat diffusivity, respectively. The magnitude of the constant horizontal turbulent viscosity term ($A_H = 50,000 \text{ cm}^2/\text{sec}$) is determined by numerical consideration not by physics.

The vertical turbulent viscosity coefficient, A_V, is given by

$$A_V = \text{MAX} \left[E_v (1 - R_i/R_c), A_{Vo} \right], R_i = 0 \text{ if } R_i \leq 0 \text{ and } E_v = 10 \times A_{Vo}$$

and vertical heat diffusion coefficient, K_V, is given by

$$K_V = \text{MAX} \left[D_v (1 - R_i/R_c), K_{Vo} \right], R_i = 0 \text{ if } R_i \leq 0 \text{ and } D_v = 10 \times K_{Vo}$$

where R_c is a critical Richardson number equal to 0.25 and R_i is the local Richardson number. For most of the solutions, the background vertical turbulent viscosity, $A_{Vo} = 20 \text{ cm}^2/\text{sec}$ and the background heat diffusivity, $K_{Vo} = 2 \text{ cm}^2/\text{sec}$.

The forcing functions in Eqs. (2) and (5) are defined as

$$F_v = - \frac{\partial}{\partial z} A_V \frac{\partial V_i}{\partial z} - A_H \frac{\partial^2 V_i}{\partial x^2}, \tag{7}$$

$$F_\rho = - \frac{\partial}{\partial z} K_V \frac{\partial T_i}{\partial z} - K_H \frac{\partial^2 T_i}{\partial x^2}. \tag{8}$$

Where V_i and T_i are initial velocity and temperature field, respectively. With these body forces and the additional boundary conditions below, the initial state remains in geostrophic and hydrostatic equilibrium because the body forces cancel the horizontal and vertical diffusion of the initial flow's momentum and heat. These body forces maintain the initial flow fields as long as possible after the flow fields deviate from equilibrium by applied surface wind stress.

In order to eliminate pressure from Eq. (1) and (3) we define a stream function, ψ,

$$-\psi_z = u \quad \text{and} \quad \psi_x = w,$$

the vorticity, η, becomes

$$\eta = -\nabla^2 \psi.$$

Taking the curl of Eq. (1) and (3) yields the vorticity equation,

$$\frac{\partial}{\partial t} \eta + \mathbf{J}(\psi, \eta) - f v_z - g \frac{\rho_x}{\rho_o} =$$
$$\left(\frac{\partial^2}{\partial z^2} - \frac{\partial}{\partial x^2} \right) \left(A_V \left[\frac{\partial u}{\partial z} + \frac{\partial w}{\partial x} \right] \right) - \frac{\partial^2}{\partial x \partial z} \left(A_V \frac{\partial w}{\partial z} \right) + A_H \frac{\partial^3}{\partial z \partial x^2} u \tag{9}$$

where $\mathbf{J}$ is the Jacobian operator. This vorticity equation (9) together with Eqs. (2) and (5) is integrated forward in time.

b. Boundary conditions. Periodic boundary conditions are used at $x = 0$ and $x = L$. The vertical boundary conditions are prescribed as

$$A_V \left[\frac{\partial u}{\partial z} + \frac{\partial w}{\partial x} \right] = \tau_x \text{ at } z = 0$$

$$A_V \frac{\partial v}{\partial z} = \tau_y \text{ at } z = 0$$

$$w = \psi = 0 \quad \text{at} \quad z = 0 \quad \text{and} \quad z = -H$$

$$K_V \frac{\partial T}{\partial z} = 0 \quad \text{at} \quad z = 0 \quad \text{and} \quad z = -H$$

$$A_V \frac{\partial v}{\partial z} = A_V \left[\frac{\partial u}{\partial z} + \frac{\partial w}{\partial x} \right] = 0 \quad \text{at} \quad z = -H$$

where H is the depth of the model domain. The initial states of V_i and T_i have finite stress and heat flux at the surface and the bottom. These small stresses and fluxes are introduced as additional boundary conditions that are required to maintain the initial state in the absence of wind stress.

Vanishing ψ at $z = 0$ and $-H$ requires that a pressure gradient, $\partial \hat{P}/\partial y$, be introduced in order to create a steady state solution. This can be seen by integrating Eq. (2) over the domain using boundary conditions and the periodicity of the flow:

$$\frac{1}{\rho_o} \frac{\partial \hat{P}}{\partial y} = \frac{\tau_y}{H}. \tag{10}$$

Physically, an Ekman transport is forced by the wind in the upper mixed layer in the x direction. Since no net transport is allowed (i.e., ψ vanishes in both boundaries), a vertical uniform geostrophic current in the x direction results which balances the Ekman transport.

c. Initial jet. Because our domain is periodic in x, the shape of the initial flow is two jets flowing in opposite directions and separated by 20 km. The initial velocity and temperature fields, V_i and T_i, respectively, are the exact solutions of the governing equations without wind stress,

$$V_i = \left[V_o \times \exp \left\{ - \left(\frac{x - 10 \text{ km}}{3.0 \text{ km}} \right)^2 \right\} - V_o \times \exp \left\{ - \left(\frac{x - 30 \text{ km}}{3.0} \right)^2 \right\} \right] \left(\frac{(H + z)}{H} \right) \tag{11}$$

$$T_i = \frac{V_o \times \sqrt{\pi} f}{1.5 \text{ km} \times H} \left(\text{erf} \left(\frac{x - 10 \text{ km}}{3.0 \text{ km}} \right) - \text{erf} \left(\frac{x - 30 \text{ km}}{3.0 \text{ km}} \right) \right) + \left(10.0 + 6.0 \times \frac{z}{H} \right) \tag{12}$$

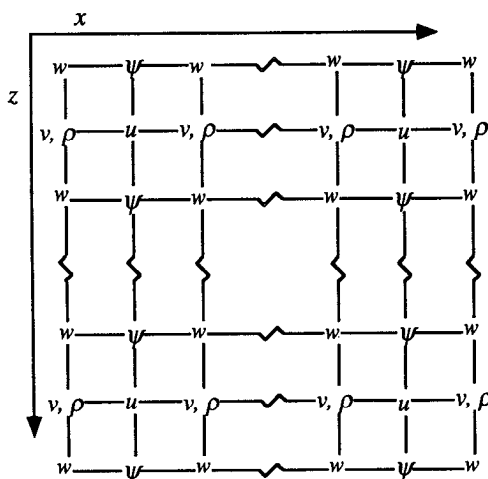where erf is the error function, and V_o is the maximum speed of the jet. In addition to

Figure 1. The staggered grid map used in the model.

the temperature change forced by V_i, there is a basic linear stratification of 6°C over the vertical extent of the domain. The initial circulation field is geostrophically balanced and is maintained by the friction and diffusion by a body force introduced into the fluid. The initial temperature and velocity fields are shown in Figure 2.

d. Numerical technique. Eqs. (2) and (5) are solved using centered finite differences in space and time. A forward time scheme is used every 66 time steps to eliminate time-splitting of the solutions. The vertical and horizontal diffusion terms are always lagged one time step. A staggered Arakawa C grid scheme in space is used (Fig. 1). Eq. (19) is solved by a numerical Poisson solver using the FFT method (Wilhelmson and Eriksen, 1977). A time step of one minute is used in all experiments. The forced convective adjustment method is used in the model to avoid unrealistic, unstable negative density gradients.

3. Results

This study addresses the following questions: How does the presence of a jet influence an Ekman layer driven by a uniform wind? What are the characteristics of the secondary circulation patterns which result from the interaction between a jet and a wind stress field? What effect does the wind-jet interaction within the mixed-layer have on the vertical velocity field? And, what role does this vertical velocity field play in transporting heat and momentum across the mixed-layer?

Seven experiments were performed with varying wind stresses ($\tau_y = 1$, 2 and 0.1 dyne/cm^2, $\tau_x = 1$ dyne/cm^2) and maximum initial jet velocities ($V_o = 6$ and 30 cm/s). The semi-linear version of the model with weak wind stress ($\tau_y = 0.1$) was

Initial Field
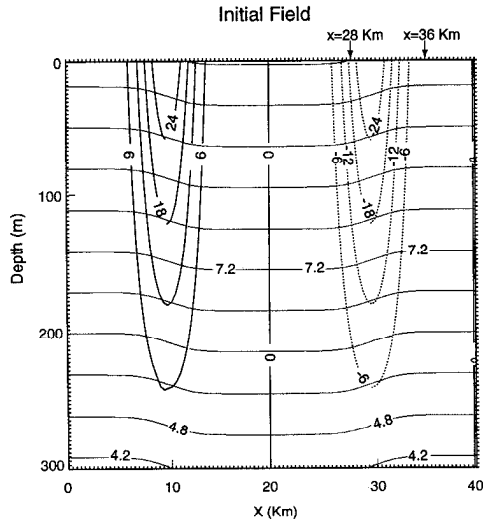

Figure 2. Initial velocity (cm/sec) and temperature (°C) field. The x positions for Figures 3 and 4 are also marked.

also integrated to identify the nonlinear effects in a weakly forced situation. The wind stress and maximum initial jet velocities used in the seven experiments are tabulated in Table 1.

a. Near-inertial motion. When a wind stress is applied, an Ekman layer forms and near-inertial motions set up. The reader may consult the extensive derivation of the dispersion relation of near-inertial waves in the presence of geostrophic shear by Kunze (1985). The wind-generated near-inertial motions vary depending upon the sign of relative vorticity and the direction of wind stress. Using numerical ray theory, Kunze (1985) found that subinertial waves become trapped in regions of negative relative vorticity. According to his analysis, spatial variations in the effective Coriolis frequency influence the propagation behavior of near-inertial waves. These waves reflect at turning points in the horizontal direction as the horizontal component of a

Table 1. The wind stress and maximum initial jet velocities used in the experiments.

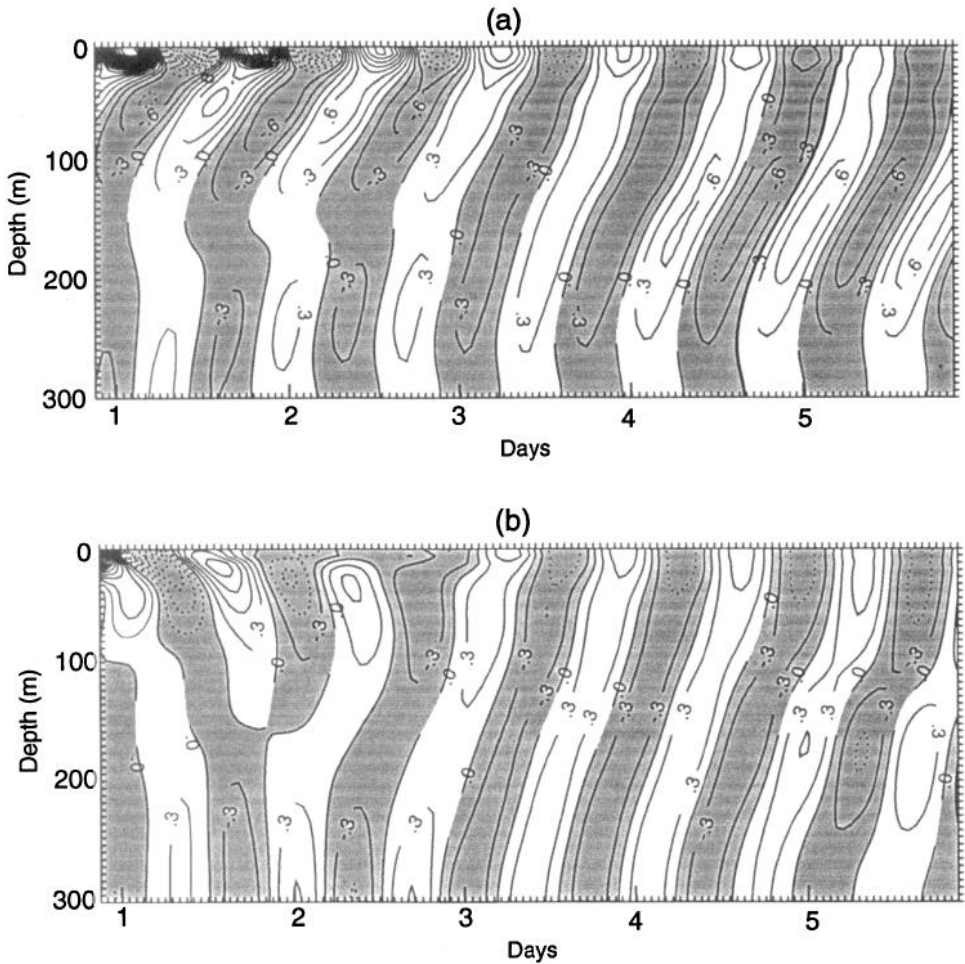| Experiment #	τ_x (dyne/cm^2)	τ_y (dyne/cm^2)	V_o (cm/sec)	Max R_o	Dynamics
1	0.0	1.0	30	0.80	Nonlinear
2	1.0	0.0	30	0.80	Nonlinear
3	0.0	2.0	30	0.80	Nonlinear
4	0.0	1.0	6	0.16	Nonlinear
5	0.0	0.1	30	0.80	Nonlinear
6	0.0	0.1	30	0.80	Semi-linear
7	0.0	1.0	30	0.80	Linear

Figure 3. The space-time $(z\text{-}t)$ plots of near-inertial fluctuation of v for Experiment 1 during the first six days at (a) $x = 28$ km and at (b) $x = 36$ km. The contour interval is 0.3 cm/sec.

wave vector approaches zero, which occurs at the boundaries of regions of negative relative vorticity. Observations by Kunze and Sanford (1984), Weller (1985) and Mied *et al.* (1986) show enhanced near-inertial energy levels on the negative vorticity sides of fronts. In our model, with wind forcing parallel to the jet, the near-inertial wave energy propagates downward (with upward phase propagation) in the positive vorticity regions that appear to slowly dissipate. To show these subinertial wave motions, high passed (cut-off frequency of one cycle per day) space-time $(z\text{-}t)$ plots of jets are presented in Figure 3 for Experiment 1. Initially, in the positive vorticity region, a downward phase propagation appears in the upper 100 m. But, after two
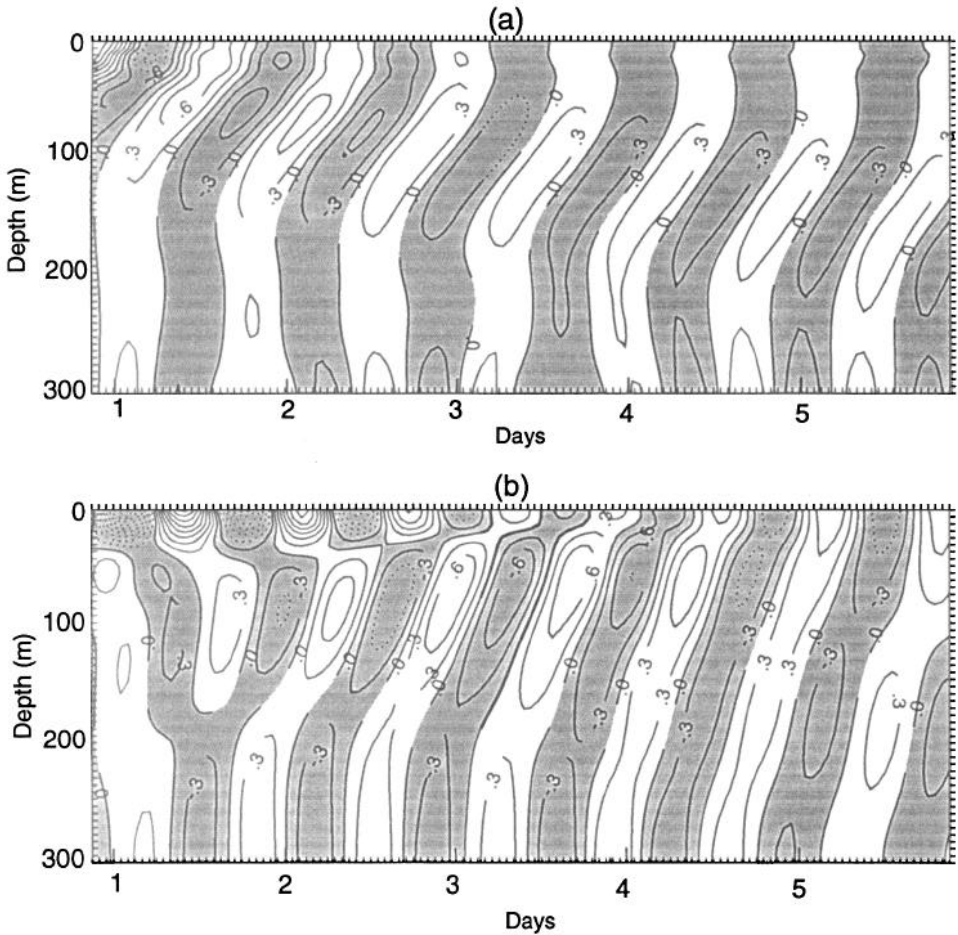
Figure 4. The space-time $(z\text{-}t)$ plots of near-inertial fluctuation of v for Experiment 2 during the first six days at (a) $x = 28$ km and at (b) $x = 36$ km. The contour interval is 0.3 cm/sec.

and a half days, the inertial energy propagates downward with an upward phase propagation. After the onset of wind in the negative vorticity region, the near-inertial energy remains trapped in the upper 200 m and is four times larger than that observed in the positive vorticity region.

When the wind direction changes from parallel to the jet to perpendicular to the jet (Experiment 2, Fig. 4), the trapping depth of subinertial waves slowly becomes deeper in the negative vorticity region. In the positive vorticity region, the direction of subinertial wave phase propagation is upward in the initial four days of simulation. The near-inertial energy maximum averaged over the first three inertial days decreases by a factor of two when the wind changed from parallel to the jet to
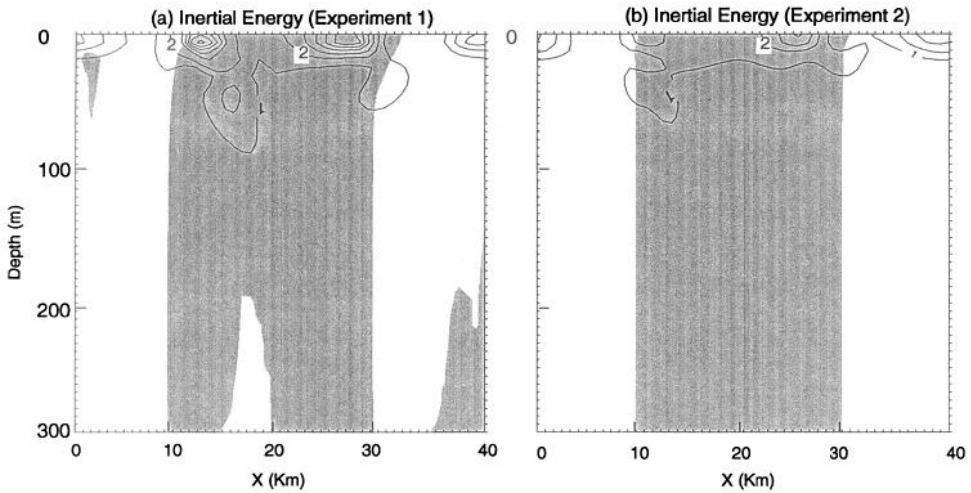
Figure 5. Mean near-inertial energy of the first three days for (a) Experiment 1 and (b) Experiment 2. Negative vorticity regions calculated from the mean field are shaded. The contour interval is 1.0 cm²/sec².

perpendicular to the jet (Fig. 5). Thus, the initial amplitude of near-inertial motion depends on the direction of the wind to the jet and the initial vorticity field. Figure 6 shows the inertial energy averaged over the second three days. The trapping of the inertial waves in the negative vorticity region occurs when the wind is both parallel and perpendicular to the jet, thus creating a broad high-inertial energy area in the
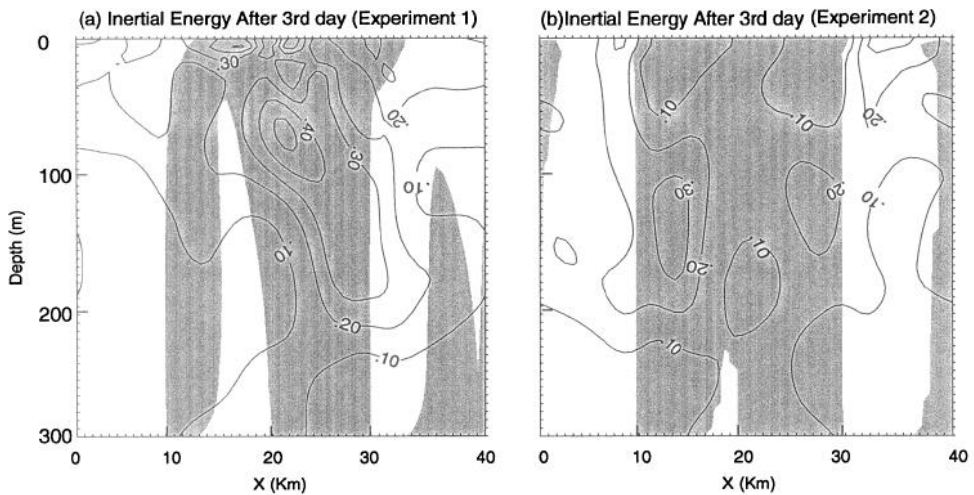

Figure 6. Same as Figure 5 except near-inertial energy is averaged over the second three days. The contour interval is 0.1 cm²/sec².
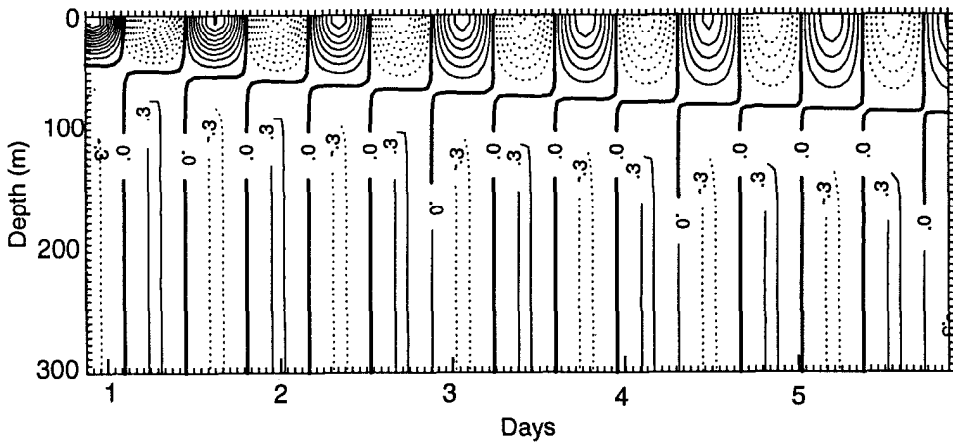
Figure 7. The space-time $(z\text{-}t)$ plot of near-inertial fluctuation of v for the linear model (Experiment 7) at $x = 28$ km. The contour interval is 0.3 cm/sec.

upper 200 m. For both cases, the inertial energy transfer from the surface to the deep layer is intensive in the positive relative vorticity regions.

D'Asaro's (1985) observations show that significant decay of inertial motions in the mixed layer occurs within a few inertial periods. This decay in inertial motions occurs due to the β-effect which reduces the north-south scales of the motion and thus enhances vertical propagation (D'Asaro, 1989). Our model simulation shows that rapid vertical propagation can result without β-effect in an ocean with initial relative vorticity. The linear solution (Experiment 7), which is described in the Appendix, does not show any vertical propagation (Fig. 7). Thus, the presence of relative vorticity and nonlinear momentum transport $(w'dv'/dz)$ are required to induce inertial wave leakage from the mixed layer. Our model simulations demonstrate that the downward energy propagation causes the rapid decay of initial near-inertial response to the wind in the mixed layer. Wang's (1991) channel flow model also shows the dependency of the near-inertial wave propagation property to the sign of the vorticity in the presence of ambient geostrophic flow.

The behavior of inertial motions in the mixed layer in several of our experiments is shown on Figure 8. The inertial oscillation in the surface persists for a very long time for the linear model (heavy solid line) but the inertial oscillation nearly disappears after four days in the case of the nonlinear model with wind blowing in the direction of the jet (light solid line). The inertial amplitude motion is larger in the linear model that in the nonlinear model with the same parameters. In general, the amplitude of the inertial oscillation throughout the domain is larger in the case of wind parallel to the jet than in the case of wind perpendicular to the jet.
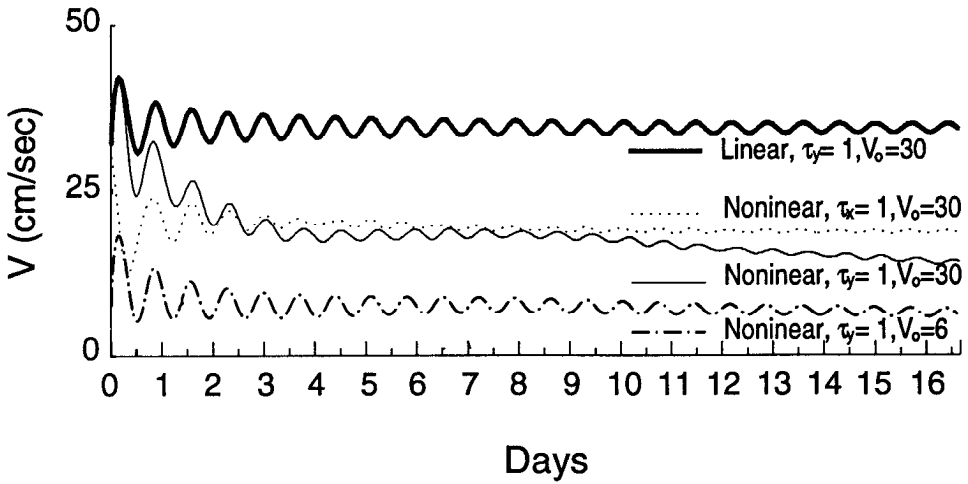
Figure 8. Time plots of v at $x = 10$ km for Experiment 1 (solid line), for Experiment 2 (dotted line). For Experiment 4 (dot-dashed line) and for Experiment 7 (heavy solid line).

b. Energetics. We divide the fields into a time mean over several inertial oscillations and a deviation from that mean:

$$\psi = \bar{\psi}(x, z) + \psi'(x, z, t)$$
$$u = \bar{u}(x, z) + u'(x, z, t)$$
$$v = \bar{v}(x, z) + v'(x, z, t)$$
$$w = \bar{w}(x, z) + w'(x, z, t)$$
$$\rho = \bar{\rho}(x, z) + \rho'(x, z, t)$$
$$\eta = \bar{\eta}(x, z) + \eta'(x, z, t).$$

After dropping terms that integrate to zero over the model domain, the time mean equation of (12) is

$$\frac{\partial}{\partial t}\bar{\eta} + \mathbf{J}(\overline{\psi', \eta'}) - f\bar{v}_z = \frac{\partial^2}{\partial z^2}\left(\bar{A}_v \frac{\partial \bar{u}}{\partial z}\right) + \frac{\partial^2}{\partial z^2}\left(\overline{A'_v \frac{\partial u'}{\partial z}}\right). \tag{13}$$

Subtracting Eq. (13) from Eq. (12) gives the perturbation vorticity equation,

$$\frac{\partial}{\partial t}\eta' + \psi'_x\overline{\eta_z} - \bar{\psi}_z\eta'_x - \mathbf{J}(\overline{\psi', \eta'}) + \mathbf{J}(\psi', \eta') - fv'_z - g\frac{\rho'_x}{\rho_o}$$

$$= \left(\frac{\partial^2}{\partial z^2} - \frac{\partial}{\partial x^2}\right)\left(A'_v \frac{\partial \bar{u}}{\partial z} + \bar{A}_v\left[\frac{\partial u'}{\partial z} + \frac{\partial w'}{\partial x}\right] + A'_v \frac{\partial u'}{\partial z}\right) \tag{14}$$

$$- \frac{\partial^2}{\partial z^2}\left(\overline{A'_v \frac{\partial u'}{\partial z}}\right) - \frac{\partial^2}{\partial x \partial z}\left(A'_v \frac{\partial w'}{\partial z} + A'_v \frac{\partial \bar{w}}{\partial z} + \bar{A}_v \frac{\partial w'}{\partial z}\right) + A_H \frac{\partial^3}{\partial z \partial x^2}u'.$$

Multiplying Eq. (14) by ψ', integrating over the model domain and averaging over time, results in the following perturbation energy equation for u'^2 and w'^2.

$$\iint \overline{\frac{1}{2}\frac{\partial}{\partial t}(u'^2 + v'^2)}\,dxdz$$

$$= -\iint \left[\overline{(u'u' + u'w')\frac{\partial \bar{u}}{\partial x}} + \overline{(w'w' + u' + w')\frac{\partial \bar{w}}{\partial z}}\right]dxdz$$

$$+ g\iint \overline{\psi'\frac{\rho'_x}{\rho_o}}\,dxdz + A_H\iint \overline{\psi'\frac{\partial^3}{\partial z\partial x^2}u'}\,dxdz \tag{15}$$

$$+ \iint \overline{\psi'\left(\frac{\partial^2}{\partial z^2} - \frac{\partial}{\partial x^2}\right)\left(A'_V\frac{\partial \bar{u}}{\partial z} + \bar{A}_V\left[\frac{\partial u'}{\partial z} + \frac{\partial w'}{\partial x}\right] + A'_V\frac{\partial u'}{\partial z}\right)}\,dxdz$$

$$- \iint \overline{\psi'\frac{\partial^2}{\partial x\partial z}\left(A'_V\frac{\partial w'}{\partial z} + A'_V\frac{\partial \bar{w}}{\partial z} + \bar{A}_V\frac{\partial w'}{\partial z}\right)}\,dxdz.$$

In a similar fashion, the perturbation v'^2 energy equation becomes:

$$\iint \overline{v'\frac{\partial v'}{\partial t}}\,dxdz = -\iint \overline{u'v'\bar{v}_x}\,dxdz - \iint \overline{v'w'\bar{v}_z}\,dxdz - \iint \overline{fu'v'}\,dxdz$$

$$+ \iint \overline{v'\frac{\partial}{\partial z}\left[(\bar{A}_V + A'_V)\frac{\partial v'}{\partial z}\right]}\,dxdz \tag{16}$$

$$+ \iint \overline{v'\frac{\partial}{\partial z}\left[A'_V\frac{\partial \bar{v}}{\partial z}\right]}\,dxdz + A_H\iint \overline{v'\frac{\partial^2}{\partial x^2}v'}\,dxdz.$$
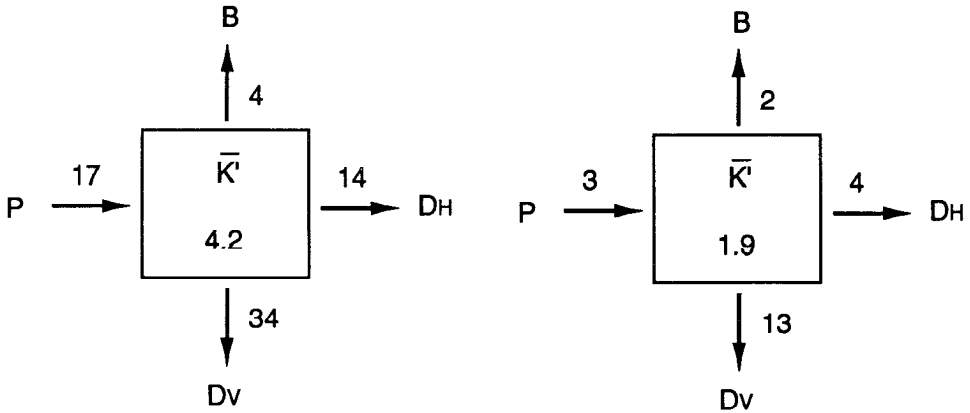
Adding Eq. (15) to Eq. (16) yields the total energy equation,

$$\iint \overline{\frac{1}{2}\frac{\partial}{\partial t}(u'^2 + v'^2 + w'^2)}\,dxdz = B + P + D_V + D_H. \tag{17}$$

where the turbulent energy production is given by

$$P = \iint \left[\overline{(u'u' + u'w')\frac{\partial \bar{u}}{\partial x}} + \overline{(w'w' + u'w')\frac{\partial \bar{w}}{\partial z}} + \overline{u'v'\frac{\partial \bar{v}}{\partial x}} + \overline{v'w'\frac{\partial \bar{v}}{\partial z}}\right]dxdz,$$

the vertical diffusion of energy by

$$D_V = \iint \overline{\psi'\left(\frac{\partial^2}{\partial z^2} - \frac{\partial}{\partial x^2}\right)\left(A'_V\frac{\partial \bar{u}}{\partial z} + \bar{A}_V\left[\frac{\partial u'}{\partial z} + \frac{\partial w'}{\partial x}\right] + A'_V\frac{\partial u'}{\partial z}\right)}\,dxdz$$

$$- \iint \overline{\psi'\frac{\partial}{\partial x\partial z}\left(A'_V\frac{\partial w'}{\partial z} + A'_V\frac{\partial \bar{w}}{\partial z} + \bar{A}_V\frac{\partial w'}{\partial z}\right)}\,dxdz$$

$$+ \iint \overline{v'\frac{\partial}{\partial z}\left[(\bar{A}_V + A'_V)\frac{\partial v'}{\partial z}\right]}\,dxdz + \iint \overline{v'\frac{\partial}{\partial z}\left[A'_V\frac{\partial \bar{v}}{\partial z}\right]}\,dxdz,$$

T_y = 1 dyne/cm² (Experiment 1) T_x = 1 dyne/cm² (Experiment 2)

Figure 9. Fluctuation energy (cm²/sec²) and its flux (10^{-3} cm²/sec³) diagram. $\overline{K'}$ is the averaged fluctuation energy. See text for the definition of flux terms.

the horizontal diffusion of energy by

$$D_H = A_H \iint \overline{\psi' \frac{\partial^3}{\partial z \partial x^2} u'} \, dxdz + A_H \iint \overline{v' \frac{\partial^2}{\partial x^2} v'} \, dxdz.$$

and the turbulent energy flux by buoyancy is defined as,

$$B = g \iint \overline{\psi' \frac{\rho'_x}{\rho_o}} \, dxdz.$$

The averaged energy diagram for Experiment 1 and 2 is shown in Figure 9. The averaging time period is four inertial periods after integrating the model one inertial period. In both experiments, vertical diffusion is much larger than the horizontal diffusion. The turbulent energy production term, P, from mean horizontal and vertical shear, is about six times larger in the case of Experiment 1 than in the case of Experiment 2. The averaged turbulent energy when the wind is perpendicular to the jet is about half that when the wind is parallel to the jet.

c. *Mean circulation after 6 days.* The mean vertical velocity contours for Experiment 1–4, after near inertial motions are set up throughout the water column, averaged from day 10 to day 17 are shown in Figure 10. With $\tau_y \geq 1$ dyne/cm², strong downwelling regions form in the subsurface layer of the negative vorticity region. The upwelling regions within the mixed-layer form when the jet is downwind, but, below the mixed layer, when the jet is upwind. The largest magnitude in the vertical velocity field due to wind-jet interactions occurs when the jet is upwind. Vertical advection
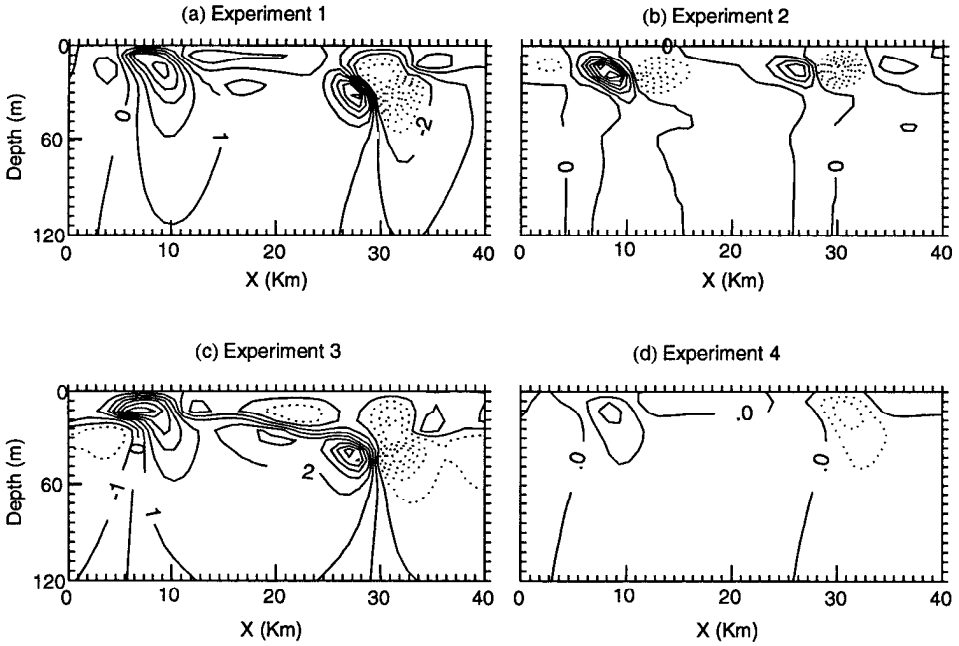
Figure 10. Mean vertical velocity w averaged over 10 days after 6 days of integration for (a) Experiments 1, (b) Experiment 2, (c) Experiment 3 and (d) Experiment 4. The contour interval is 1 m/day.

cells with a magnitude of 8.6 m/day occur for Experiment 1 and 1.4 m/day for Experiment 2. The strong wind (Experiment 3) significantly alters the shape of initial jet (Fig. 11 and 12). Upwelling increases slightly from an average of 5.4 m/day to 6.8 m/day, and downwelling decreases from 8.6 m/day to 7.1 m/day. The strength of the initial jet (the magnitude of Rossby number) is more important than the strength of the wind stress, which indicates that the wind-driven secondary circulation is mainly caused by the presence of the vertical and horizontal shear.

The depth of the secondary circulation is very shallow. The mean y component of velocity ($\bar{v}$) and its change from the initial field ($\bar{v} - V_i$) are shown in Figures 11 and 12, respectively. When a wind stress perpendicular to the jet is applied (Experiment 2), the wind-jet interaction occurs primarily within the mixed layer. The change is very shallow and small compared to other cases.

d. Semi-linear model. A semi-linear model is integrated to dramatize the nonlinear effects. The equations for the semi-linear model are:

$$\frac{\partial u}{\partial t} - fv = -\frac{1}{\rho_o}\frac{\partial P}{\partial x} + \frac{\partial}{\partial z}\left(A_V\left[\frac{\partial u}{\partial z} + \frac{\partial w}{\partial x}\right]\right) + A_H\frac{\partial^2 u}{\partial x^2} \tag{18}$$
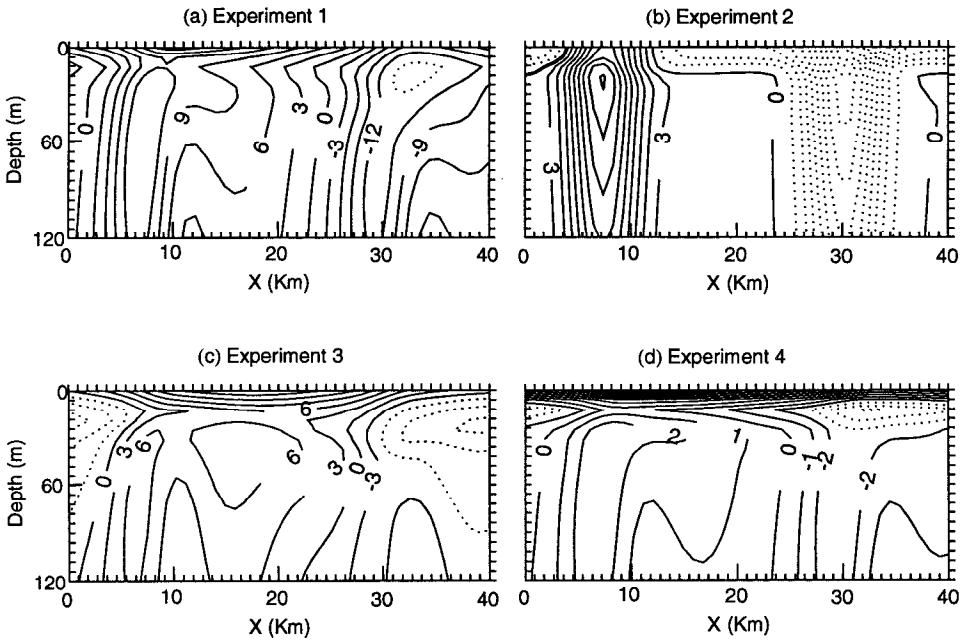
Figure 11. Mean horizontal velocity v averaged over 10 days after 6 days of integration for (a) Experiments 1, (b) Experiment 2, (c) Experiment 3 and (d) Experiment 4. The contour interval is 3 cm/sec.

$$\frac{\partial v}{\partial t} + u \frac{\partial V_i}{\partial x} + w \frac{\partial V_i}{\partial z} + fu = -\frac{1}{\rho_o}\frac{\partial \hat{P}}{\partial y} + \frac{\partial}{\partial z} A_V \frac{\partial v}{\partial z} + A_H \frac{\partial^2 v}{\partial x^2} + F_v. \qquad (19)$$

The corresponding equations for w and ρ are Eqs. (3) and (5) without the nonlinear advection terms. A weak wind stress ($\tau_y = 0.1$ dyne/cm^2) is used to force the semi-linear model experiments (Experiments 5 and 6). Because these semi-linear equations appear to contain a time increasing mode, a strong time-increasing vertical circulation cell results. The semi-linear model is valid only for a small wind stress (see Appendix). We expected the secondary circulation to obey the nearly linear equations. But, even for very mild wind events in the ocean, the interaction is still very nonlinear. The circulation cells have similar shapes for both nonlinear and semi-linear motions, but, the amplitude of the nonlinear motion is 56% of the semi-linear motion. The wind accelerates the surface flow in the semi-linear case but decelerates it in the nonlinear case (Fig. 13). The depth of the generated secondary circulation of the semi-linear model is much deeper than that of the fully nonlinear model.

The semi-linear equations are those that are known to exhibit "symmetric instabilities." The character of these instabilities is that they tend to have overturning, non-hydrostatic cells in the area where the potential vorticity of the basic flow is
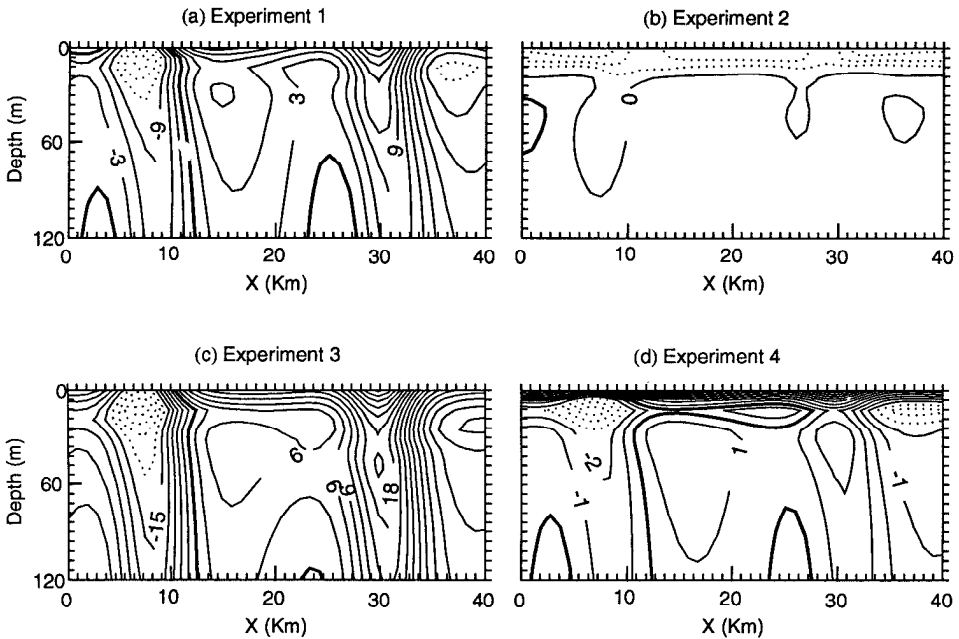
Figure 12. $\bar{v} - V_i$ for (a) Experiments 1, (b) Experiment 2, (c) Experiment 3 and (d) Experiment 4. The contour interval is 3 cm/sec.

small, i.e., in the negative shear zone. A slowly time increasing circulation is identified as a symmetric instability of the semi-linear system (Stone, 1971).

4. Discussion

For analysis of the dynamics of the secondary circulation, we used a diagnostic equation of w. This is the vertical integral of the vorticity equation and results in an "Ekman vertical velocity" equation for w when only an Ekman layer is present. It is derived by taking $\partial/\partial x$ of Eq. (2) and substituting it for $\partial u/\partial x$ from Eq. (4) and
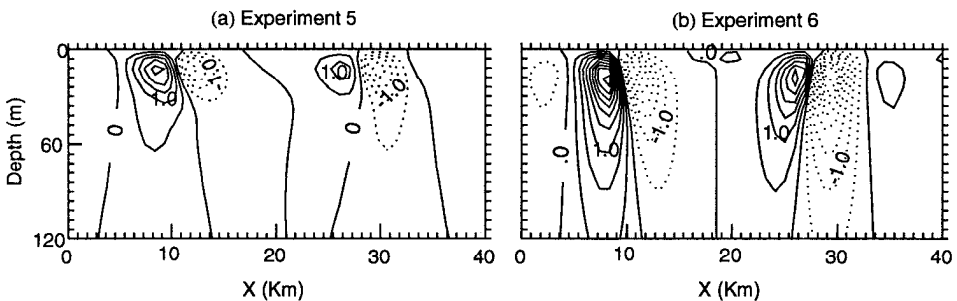

Figure 13. Mean vertical velocity w averaged over 10 days after 6 days of integration for (a) Experiment 5) and (b) Experiment 6. The contour interval is 0.5 m/day.

integrating from $-z$ to the surface:

(i)   (ii) (iii)   (iv)

$$w = \frac{\partial}{\partial x} \int_{-z}^{0} \left(\frac{\frac{\partial}{\partial z} A_V \frac{\partial v}{\partial z} - \frac{\tau_y}{H}}{\left(f + \frac{\partial v}{\partial x} \right)} \right) dz' - \frac{\partial}{\partial x} \int_{-z}^{0} \left(\frac{\frac{\partial v}{\partial t} + w \frac{\partial v}{\partial z}}{\left(f + \frac{\partial v}{\partial x} \right)} \right) dz' + \frac{\partial}{\partial x} \int_{-z}^{0} \left(\frac{A_H \frac{\partial^2 v}{\partial x^2} - F_v}{\left(f + \frac{\partial v}{\partial x} \right)} \right) dz'.$$

(20)

The vertical velocity is forced primarily by: (i) the x-dependence of turbulent vertical mixing of momentum in the Ekman layer, (ii) the acceleration of flow, (iii) nonlinear vertical advection of horizontal momentum and (iv) the horizontal body forces and horizontal diffusion.

The time means of each term (over three inertial periods after integration of ten inertial periods in Eq. 39) at the center of the two jets of Experiment 1 are presented as a function of depth in Figures 14a and 14b. There are three distinctive layers in the downwelling region under the jet of upwind direction. All four terms are comparable in the surface layer. In the subsurface layer, w is caused primarily by the x-dependence of vertical mixing. Only terms proportional to diffusivities [terms (i) and (iv)] are acting in the deep layer. In the upwelling region under the downwind jet, the viscous terms are dominant; w is represented by the term (i) at the base of Ekman layer and is produced by the divergence of the Ekman layer transport from the change of the relative vorticity of the flow. For jets perpendicular to the wind (Experiment 2), w is represented by term (i), and all terms below the viscous mixed layer are very small because there is no net Ekman divergence (Fig. 14c).

The simplest diagnostics are when only vertical diffusion is acting in Eq. (20). For the steady state, and below the mixed layer where $w \partial v / \partial z$ is small, u becomes

$$u \approx \frac{\frac{\partial}{\partial z} \tau_{yz}}{(f + v_x)},$$

(21)

where τ is Reynolds stress. Then, from Eq. (4), and if variation of v in the z direction is small, w becomes

$$w \approx - \frac{\tau_{yz}|_{z=0} \times v_{xx}}{(f + v_x)^2}.$$

(22)

This simple case is presented schematically in Figure 15. When the wind blows along the jet, water is transported perpendicular to the jet. The transport is reduced in the area of positive relative vorticity and is increased in the area of negative vorticity. For the downwind case, the divergence region is formed along the axis of the jet and thus
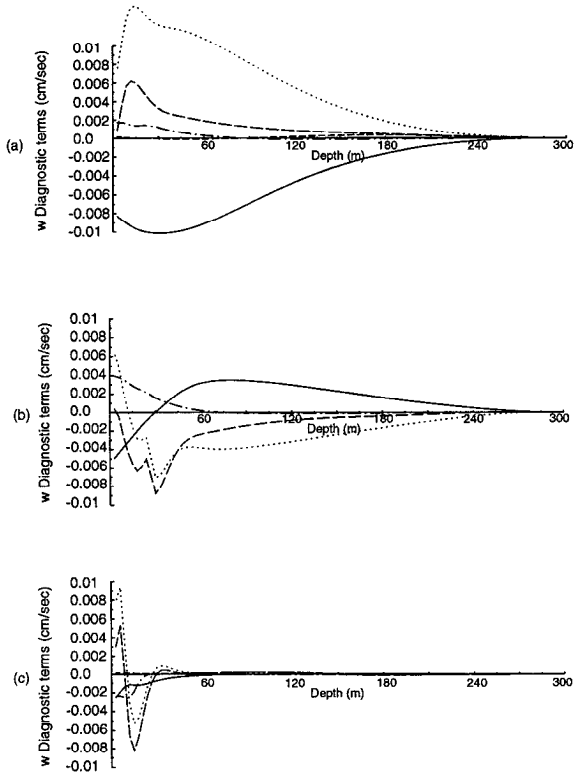
Figure 14. The vertical distribution of various terms from the w diagnostic equation averaged over four inertial periods (a) at the center of the jet of upwind direction in Experiment 1 ($x = 30$ km), (b) at the center of the jet of downwind direction in Experiment 1 ($x = 10.8$ km) and (c) at the center of jet in Experiment 2 ($x = 30$ km) after ten inertial periods (170 hours) of integration. The long dashed line is for w, the dotted line is for the term (i), short dashed line is for the term (ii), dot-dashed line is for the term (iii) and solid line is for the term (iv). See Eq. (20) in the discussion section to identify the terms.

upwelling is developed below the mixed layer. These typical vertical circulation cells are shown in Figure 16b (also see Paduan and Niiler, 1991).

Since the terms proportional to viscosity are dominant in the w diagnostic equation, we ran the model with a larger horizontal viscosity ($A_H = 500,000$ cm^2/sec, $A_{V_o} = 20$ cm^2/sec) and with a smaller vertical diffusion coefficient ($A_{V_o} = 2$ cm^2/sec, $A_H = 50,000$ cm^2/sec). Mean w contours of two additional experiments and that of Experiment 1 are shown in Figure 16. The layer depth of the high vertical mixing ($R_i < 0.25$) does not change much; but, the magnitude of w and the depth of the secondary circulation cell are quite different.

Figure 17 shows the maximum downwelling velocity as a function of the horizontal viscosity coefficient A_H. The maximum downwelling velocity rapidly increases from
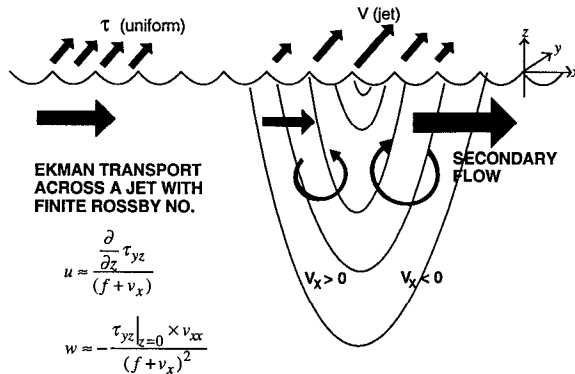
Figure 15. The schematics of the generation of secondary circulation by wind-jet interaction.

$A_H = 0$ cm^2/sec to $A_H = 250,000$ cm^2/sec, reaches the maximum value near $A_H = 500,000$ cm^2/sec and slowly decreases for A_H larger than 500,000 cm^2/sec. The shapes of the mean jet after seven days of integration were almost the same for all experiments with values of A_H above 250,000 cm^2/sec, and showed small change (± 3 cm /sec from initial ± 30 cm/sec) from the initial jet.

The vertical distribution of the four terms in Eq. (20) for Experiment 5 ($\tau_y = 0.1$ dyne /cm^2, $A_H = 50,000$ cm^2/sec), is proportionally similar to that of Experiment 1 ($\tau_y = 1.0$ dyne/cm^2) but with $A_H = 500,000$ cm^2/sec (not shown). Since both cases have same Reynolds number,

$$R = \frac{R_o \delta}{E_h} = \frac{\tau}{(A_v f)^{1/2} A_H},$$

where terms are defined in the Appendix, and the flows of both cases are dynamically similar.

We began these experiments having Eq. (22) in mind as the model for producing strong circulation below the mixed layer. However, in the simplest case of a 2½-D circulation, we came to the realization that within the present sophistication of numerical modeling, where the grid Reynolds numbers must be reduced to values no greater than 5 to avoid grid waves, the secondary circulation patterns are governed by the grid diffusivities. This was a disappointment, as it led us to the realization that the upper ocean circulation in a global eddy field of the large scale numerical model is governed very much by how the sub-grid scale is parameterized. There appears to be no escape: either we learn to understand what makes better physical bases for parameterization of horizontal sub-grid processes or we will not be able to develop our ability to model the significant element of small and mesoscale systems in a realistic way.
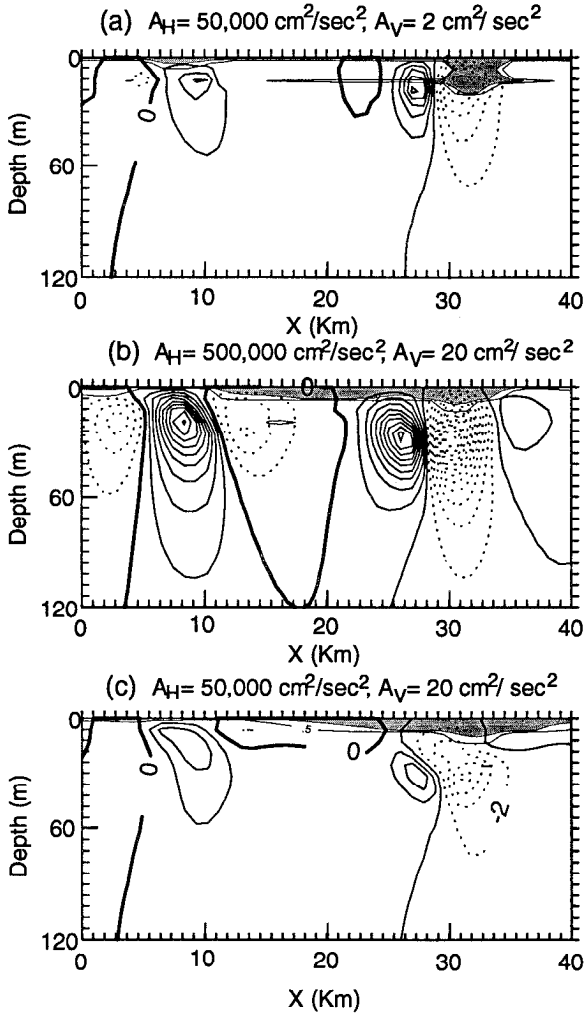
Figure 16. Mean vertical velocity w averaged over 10 days after 6 days of integration with various diffusion coefficients. The unstable areas where the Richardson number is smaller than 0.25 are shaded. The contour interval is 2.0 m/day.

5. Summary

Our calculations show that the wind-jet interactions generate significant vertical circulation. The full model for this interaction is complicated, yet several general results emerge.

The inertial oscillations do not propagate into the deep layer for the linear case as shown in Figure 13. The inertial energy of the linear case is also evenly distributed
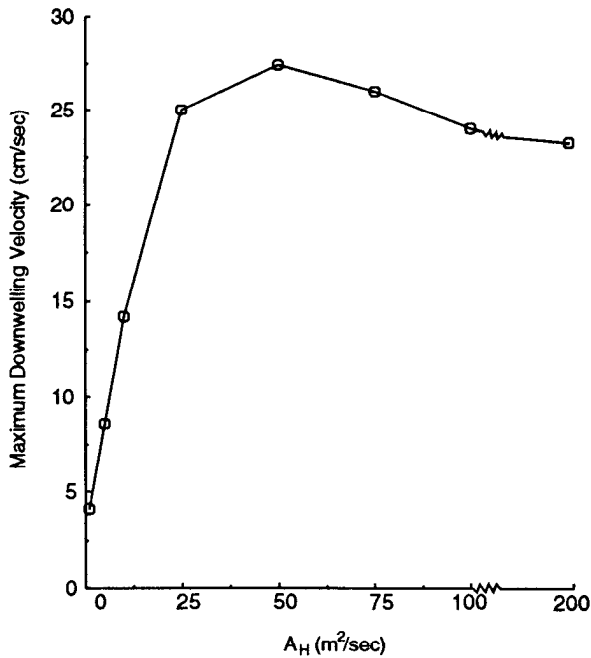
Figure 17. The maximum downwelling velocity under the jet of upwind direction as a function of the horizontal diffusion coefficient A_H.

and concentrated in the surface layer. The inertial energy leaking into the deep layer from the Ekman layer is closely related to the ambient shear or relative vorticity.

In the case of a wind perpendicular to the jet, the near-inertial motions are propagated away from the Ekman layer. In the case of a wind parallel to the jet, the near-inertial motions are continually generated by the wind-altered and geostrophically adjusted vertical shear of the mean horizontal current. The largest wind-jet interactions occur when the jet is upwind. This dependency of near-inertial behavior on wind direction is not presented by Wang's (1991) channel flow model possibly due to the presence of the horizontal boundary effects. But, Klein and Hua's (1988) quasi-geostrophic model, coupled with the analytic mixed-layer solution, shows the dependency. The observations by Paduan and Niiler (1991) strongly suggest the relation of vertical circulation to wind-jet direction.

The vertical circulation patterns and diagnostics calculations from our numerical experiments show that Ekman pumping and suction are enhanced by the horizontal shear of geostrophic jets or eddies. Even with a simple constant wind stress (i.e., no wind stress curl), the interaction of the jet and wind field produces Ekman pumping or suction.

In our simple 2½-dimensional model, the presence of geostrophic jets or eddies in mixed-layer modeling play crucial roles. The shear field is much more important than the strength of the wind stress for affecting the mixing depth and vertical circulation. A 3-D model with high vertical resolution in the upper layer is required for better understanding of the ocean response to wind in an ocean full of two dimensional jets and eddies of various size and strength. However, adding a wind-driven Ekman layer onto an eddy-resolving model does not produce a realistic circulation in the upper ocean.

APPENDIX

To demonstrate the parameter range of solutions integrated in the dimensional domain, the equation of motions are non-dimensionalized. The following nondimensional variables are introduced:

$$x* = Lx, \qquad z* = Hz,$$
$$u* = u_o u, \qquad v* = V_o(V_i + \delta v),$$
$$w* = u_o \frac{H}{L} w, \qquad p* = P*_i(x*, z*) + \rho f u_o L_p.$$

where

$$u_o = \frac{\tau/\rho}{\delta_E f},$$

$$\delta = \frac{u_o}{V_o},$$

$$fV*_i = \frac{1}{\rho_o} \frac{\partial P*_i}{\partial x*}$$

V_o is the velocity at the center of the jet, δ_E is the Ekman layer depth and H is the model depth.

When the above nondimensional variables are introduced into the steady state horizontal momentum equations, Equation (1) in nondimensional form becomes (in the case of $A_V = $ constant and $\delta_E = (A_V/f)^{1/2}$);

$$R_o \delta \left\{ u \frac{\partial u}{\partial x} + w \frac{\partial u}{\partial z} \right\} - v = - \frac{\partial p}{\partial x} + E_h \frac{\partial^2 u}{\partial x^2} + E_v \frac{\partial^2 u}{\partial z^2} \qquad (A.1)$$

Using Eqs. (6) and (24), Eq. (2) becomes

$$R_o \left\{ u \frac{\partial V_i}{\partial x} + \delta u \frac{\partial v}{\partial x} + w \frac{\partial V_i}{\partial z} + \delta w \frac{\partial v}{\partial z} \right\} + u = -E_v^{1/2} + E_h \frac{\partial^2 v}{\partial x^2} + E_v \frac{\partial^2 v}{\partial z^2}, \quad (A.2)$$

where

$$R_o = \frac{V_o}{fL}, \qquad \text{the initial Rossby number,}$$

$$E_h = \frac{A_H}{fL^2}, \qquad \text{the horizontal Ekman number,}$$

$$E_v = \frac{A_v}{fH^2} = \left(\frac{\delta_E}{H}\right)^2, \qquad \text{the vertical Ekman number.}$$

The solutions are linear for a small initial Rossby number R_o. When terms proportional to δ are neglected, a semi-linear set of equations as described in Section 3d result. In our model, the maximum initial Rossby number is between 0.2–0.8 and δ is 0.3 when τ is 1 dyne/cm^2. The vertical Ekman number based on background vertical viscosity A_{V_o} is 0.015 (with an Ekman layer depth of 4.5 m); and, the maximum vertical Ekman number based on maximum nonlinear viscosity is 0.05 (with an Ekman layer depth of 14 m). The horizontal Ekman number used in all experiments is 1.25×10^{-4}.

REFERENCES

D'Asaro, E. A. 1985. Upper ocean temperature structure, inertial currents and Richardson numbers observed during strong meteorological forcing. J. Phys. Oceanogr., 15, 943–962.

—— 1989. The decay of wind-forced mixed layer inertial oscillations. J. Geophy. Res., 94, C2, 1045–1056.

Klein, P. and B. L. Hua. 1988. Mesoscale heterogeneity of the wind-driven mixed layer: Influence of a quasigeostrophic flow. J. Mar. Res., 46, 495–525.

Kunze, E. 1985. Near-inertial wave propagation in geostrophic shear. J. Phys. Oceanogr., 14, 544–565.

Kunze, E. and T. B. Sanford. 1984. Observations of near-inertial waves in a front. J. Phys. Oceanogr., 14, 566–581.

Mied, R. P., C. Y. Shen, C. L. Trump and G. J. Lindemann. 1986. Internal inertial waves in a Sargasso Sea Front. J. Phys. Oceanogr., 16, 1751–1762.

Niiler, P. P. 1969. On the Ekman divergence in an oceanic jet. J. Geophy. Res., 74, 7048–7052.

Paduan, J. D. and P. P. Niiler. 1991. A Lagrangian description of motion in northern California coastal transition filaments. J. Geophys. Res., 95, 18095–18109.

Pollard, R. T., P. B. Rhines and R. O. R. Y. Thomson. 1973. The deepening of the wind mixed layer. Geophys. Fluid Dyn., 3, 381–404.

Stone, P. H. 1971. Baroclinic stability under non-hydrostatic conditions. J. Fluid Mech., 45, 659–671.

Wang, D.-P. 1991. Generation and propagation of inertial waves in the subtropical front. J. Mar. Res., 49, 619–633.

Weller, R. A. 1982. The relation of near-inertial motions observed in the mixed layer during the JASIN (1978) experiments to the local wind stress and to the quasi-geostrophic flow field. J. Phys. Oceanogr., *12*, 1122–1136.

—— 1985. Near-inertial velocity variability at inertial and subinertial frequencies in the vicinity of the California Current. J. Phys. Oceanogr., *15*, 372–385.

Wilhelmson R. B. and J. H. Eriksen. 1977. Direct solution for Poisson's equation in three dimensions. J. Comp. Phys., 25, 319–331.